Coupled-mode theory for low-crosstalk higher-order modes of optical waveguides

Panu Hildén,* Fahmy Yousry, and Andriy Shevchenko
Department of Applied Physics, Aalto University, P.O. Box 13500, Aalto FI-00076, Finland

(Received 8 August 2025; accepted 23 November 2025; published 16 December 2025)

Optical crosstalk between waveguides limits the miniaturization of photonic integrated circuits. Recently, it has been shown that, using higher-order modes, the crosstalk can be significantly reduced not only between neighboring waveguides, but also between other photonic components, such as waveguide couplers and interferometers. This opens the possibility of further miniaturization of photonic chips. Here, we present a theoretical approach to investigate the peculiar properties of these low-crosstalk modes. The approach includes a semianalytical method for computing the long-range coupling coefficients of the modes. It allows us to study the dependence of light propagation on these coefficients in both finite and infinite waveguide arrays. Our findings shed light on the crosstalk suppression mechanism and intriguing discrete diffraction phenomena realizable in waveguide arrays using higher-order modes.

DOI: 10.1103/9prf-1ldr

I. INTRODUCTION

Photonic integrated circuits are a rapidly advancing technology with significant potential for future applications, owing to the low losses and large bandwidths of photonic devices in comparison with their electronic counterparts [1–3]. Moreover, silicon-based photonic chips benefit from the highly developed fabrication techniques also used by the CMOS industry [4,5]. However, photonic circuits have a major drawback that is a large footprint required to accommodate for the long wavelength of light at optical frequencies [6]. Crucially, optical signals routed in photonic chips using waveguides exhibit crosstalk due to the evanescent tails of the guided modes [7]. The crosstalk can hinder the performance of various photonic devices, such as wavelength division multiplexers [8], light detection and ranging devices (LIDARs) [9], and optical neural networks [10].

Researchers have developed several strategies for overcoming the problem of crosstalk in photonic circuits, using, e.g., nanophotonic cloaking [6], waveguide superlattices [11–13], anisotropic claddings/substrates [14,15], or deliberately bent waveguides [16–18]. Recently, it has been shown that the use of higher-order modes can significantly lower or even completely cancel crosstalk in a waveguide array [19]. These low-crosstalk higher-order modes can be readily excited by light coupled to a chip and then be utilized in various common building blocks of photonic circuits, such as Mach-Zehnder interferometers, opening an avenue for miniaturization of on-chip photonic devices [20]. The crosstalk suppression using higher-order modes can be attributed to a reduction in optical coupling between the adjacent waveguides. Consequently, the coupling between more distant waveguides can have a dominating contribution to the overall crosstalk, as does the low self-coupling of the edge waveguides in an array [20]. Moreover, when dealing with higher-order modes, the coupling between the waveguides can be negative, as shown later on in this work. The high potential for application of crosstalk reduction in on-chip photonic waveguides highlights the need for a more comprehensive investigation of this phenomenon.

Negative coupling, at which the field undergoes a phase shift of π, has been shown to occur in photonic bandgap lattices [21–23]. Light propagation in waveguide arrays with long-distance coupling has been subject to detailed theoretical investigation [24–28]. Experimentally, coupling to the second nearest waveguide has been realized by arranging the waveguides in a zigzag pattern [29]. Additionally, light has been shown to be localized in a defective waveguide at an edge of an array [30].

In this work, we show that higher-order modes can exhibit all of the aforementioned phenomena in conventional waveguides, offering a practical platform for researching the effects of discrete diffraction. The long-range coupling is especially interesting in view of the possibility to achieve optical self-collimation [25,31,32] and soliton formation [24,33]. In our studies, we employ a semianalytical method to compute long-range coupling coefficients of higher-order modes, exemplified by an azimuthally (AZ) polarized TE_{01} mode [19]. These coupling coefficients are derived from the propagation constants and field distributions of the waveguide array's eigenmodes found using the finite-element-method (FEM) solver COMSOL Multiphysics. The FEM solutions are used to construct the Hamiltonian of the system based on its eigenmode decomposition, the elements of which are the coupling coefficients in question. Our calculations show that the coupling between neighboring waveguides can be positive,

*Contact author: panu.hilden@aalto.fi

Published by the American Physical Society under the terms of the Creative Commons Attribution 4.0 International license. Further distribution of this work must maintain attribution to the author(s) and the published article's title, journal citation, and DOI.

negative, or zero, depending on the geometric parameters of the array. Considering a waveguide array with the coupling between neighboring waveguides approaching zero, we find that the coupling between more distant waveguides, as well as the waveguide self-coupling, influences the overall crosstalk. In particular, the reduced self-coupling of the edge waveguides in an array results in a phase mismatch with the other waveguides. As a result, the Hamiltonian of the system takes the form of a heptadiagonal quasi-Toeplitz matrix with perturbed corners, which can be analyzed using recent advancements in the spectral theory of such matrices [34,35]. Using these theoretical tools, we study the propagation of low-crosstalk higher-order modes and show that light can spread in the waveguide array by tunneling through every second waveguide. We also demonstrate that an AZ mode launched to an edge waveguide of an array can remain confined in that waveguide, owing to the ability of higher-order modes to form the so-called boundary-condition-dependent supermodes. Finally, we show that, in addition to suppressing crosstalk, higher-order modes can exhibit optical self-collimation, when their coupling coefficients are tuned to achieve the required mode dispersion.

II. COUPLING COEFFICIENTS OF LOW-CROSSTALK HIGHER-ORDER MODES

Consider a waveguide with a refractive index profile $\bar{n}(x, y)$ in the transverse xy plane. A bar over n or over another quantity indicates that the quantity describes an isolated waveguide, and not a waveguide array. An eigenmode of the waveguide is characterized by a transverse electric field distribution $\bar{\mathbf{e}}(x, y)$ and a propagation constant $\bar{\beta}$ that satisfy the Helmholtz equation [36]

$$\nabla_\perp^2 \bar{\mathbf{e}} + [k^2 \bar{n}^2 - \bar{\beta}^2]\bar{\mathbf{e}} = 0, \tag{1}$$

where k is the wavenumber in free space. In this work, the transverse electric and magnetic fields, denoted by $\mathbf{e}$ and $\mathbf{h}$, respectively, are normalized to satisfy the expression

$$\frac{1}{2}\iint_{-\infty}^{\infty} \mathrm{Re}\{\mathbf{e}^* \times \mathbf{h}\} \cdot \hat{\mathbf{z}} dxdy = 1, \tag{2}$$

where $\hat{\mathbf{z}}$ is the longitudinal unit vector. For a waveguide array that has N high-index cores, the refractive index is described by $\tilde{n}(x, y)$. The Helmholtz equation written for such a waveguide array,

$$\nabla_\perp^2 \tilde{\mathbf{e}} + [k^2 \tilde{n}^2 - \tilde{\beta}^2]\tilde{\mathbf{e}} = 0, \tag{3}$$

has N solutions, given by the field distributions $\tilde{\mathbf{e}}_m$ and propagation constants $\tilde{\beta}_m$ labeled with indices $m \in \{1, 2, \ldots, N\}$. These solutions, corresponding to a certain mode of a single waveguide (e.g., TE_{01}), are known as supermodes. Assuming that the evanescent fields of individual waveguides do not penetrate much into the neighboring waveguides, a supermode field $\tilde{\mathbf{e}}_m$ can be approximated by a superposition of the isolated waveguide modes:

$$\tilde{\mathbf{e}}_m = \sum_{n=1}^{N} c_{nm} \bar{\mathbf{e}}_n. \tag{4}$$

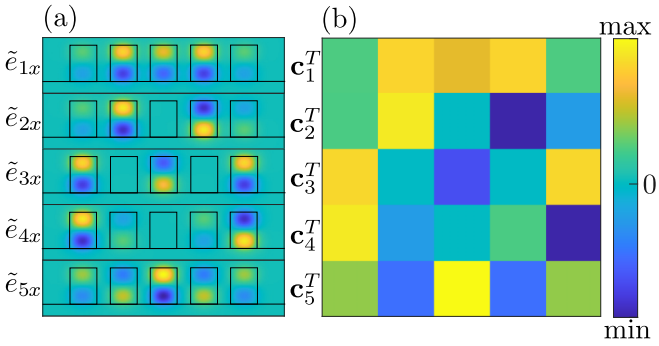


FIG. 1. (a) Supermode field distributions and (b) the vector representations of the corresponding expansion coefficients. Here, c_{nm} is defined to be positive when the upper half of the field in the transverse profile considered is positive.

Here, $\bar{\mathbf{e}}_n(x, y) = \bar{\mathbf{e}}(x - x_n, y)$ is the mode of the nth waveguide, centered at coordinate $x_n = \Lambda[n - (N + 1)/2]$, with Λ being the array period. The coefficient c_{nm} is the relative field strength in the nth waveguide for the mth supermode computed via the overlap integral [37,38]

$$c_{nm} = \frac{1}{4}\iint_{-\infty}^{\infty} (\tilde{\mathbf{e}}_m^* \times \bar{\mathbf{h}}_n + \bar{\mathbf{e}}_n \times \tilde{\mathbf{h}}_m^*) \cdot \hat{\mathbf{z}} dxdy. \tag{5}$$

As an example, Fig. 1(a) shows the x components of the electric fields for AZ-polarized supermodes in an array of five waveguides, while the matching expansion-coefficient vectors $\mathbf{c}_m = [c_{1m}\, c_{2m} \cdots c_{Nm}]^T$ are depicted in Fig. 1(b), demonstrating an excellent correspondence. The waveguides are assumed to be made of Si ($n = 3.48$) and placed on a glass substrate ($n = 1.44$) in air. Their height, width, and period are 810, 600, and 900 nm, respectively. The wavelength of light is set to 1550 nm in free space, and the modes are calculated using the COMSOL Multiphysics software (mode-analysis eigenvalue solver of the wave optics module). The choice of the geometric parameters, particularly the waveguide height, is discussed later in this work. While Eq. (4) and the coupled-mode theory can be applied not only to fundamental but also to higher-order supermodes [37,39], care must be taken while doing so, since higher-order modes of individual waveguides have more extended evanescent fields. For example, the radially polarized (RA) TM_{01} modes can also be used to suppress crosstalk [19], but they are less confined to the waveguide cores. Consequently, the gap between the waveguides needs to be larger to satisfy Eq. (4). Moreover, the crosstalk suppression of TM_{01} modes is more susceptible to fabrication errors [19], making the AZ mode a better candidate for practical applications and a better example for our demonstrations.

Assuming that a waveguide array is such that the coupled-mode theory is applicable to the higher-order modes, their propagation is described by the system of coupled differential equations [25,39]

$$-i\frac{\partial \bar{\mathbf{a}}}{\partial z} = \mathbf{H}\bar{\mathbf{a}}, \tag{6}$$

where the elements of vector $\bar{\mathbf{a}} = [\bar{a}_1\, \bar{a}_2 \cdots \bar{a}_N]^T$ are the longitudinally varying complex amplitudes of the individual waveguides; e.g., the three-dimensional field distribution of

the nth waveguide is $\bar{a}_n(z)\bar{\mathbf{e}}_n(x, y)$. Matrix $\mathbf{H}$ is the Hamiltonian of the waveguide array [40]. Its diagonal entries are the effective propagation constants of the individual waveguides, while the off-diagonal terms describe optical coupling between the waveguides. In matrix $\mathbf{H}$, the intermodal coupling between the waveguides, e.g., between RA and AZ modes, is assumed to be negligible due to the large propagation constant difference of the modes [41]. Solution to Eq. (6) takes the form [42]

$$\bar{\mathbf{a}}(z) = \mathbf{C}\mathrm{diag}(\exp i\tilde{\boldsymbol{\beta}}z)\mathbf{C}^{-1}\bar{\mathbf{a}}(0), \tag{7}$$

where the eigenvalues of the Hamiltonian, collected to the vector $\tilde{\boldsymbol{\beta}} = [\tilde{\beta}_1\ \tilde{\beta}_2 \cdots\ \tilde{\beta}_N]^T$, are the propagation constants of the supermodes, while the corresponding eigenvectors (the columns of matrix $\mathbf{C}$) are the expansion-coefficient vectors given by the overlap integral in Eq. (5). Operator diag$(\cdot)$ turns a vector into a diagonal matrix, with the nonzero elements equal to those of the vector.

The solution given by Eq. (7) can be understood as follows. The matrix transformation

$$\tilde{\mathbf{a}}(0) = \mathbf{C}^{-1}\bar{\mathbf{a}}(0) \tag{8}$$

represents the propagating field as a superposition of the supermodes instead of the fields in the individual waveguides. Being the eigenmodes of the waveguide array, the supermodes evolve upon propagation simply by accumulating the phase, such that $\tilde{a}_m(z) = \exp(i\tilde{\beta}_m z)\tilde{a}_m(0)$. The relative phases of the supermodes change upon propagation due to the differences in their propagation constants, and so does the transverse interference pattern they form. This modulates the amplitudes in the individual waveguides, which can be recovered using the inverse transformation

$$\bar{\mathbf{a}}(z) = \mathbf{C}\tilde{\mathbf{a}}(z). \tag{9}$$

To study low-crosstalk higher-order modes, we need to determine the corresponding Hamiltonian. For this, Eqs. (1) and (3) are solved numerically to obtain the propagation constants and transverse field distributions of isolated waveguides and waveguide arrays, respectively. These calculations are performed using COMSOL Multiphysics. The matrix $\mathbf{C}$ is then constructed from the overlap integrals of the numerical solutions using Eq. (5). Since the eigenvalues and eigenvectors of $\mathbf{H}$ are given by the elements of vector $\tilde{\boldsymbol{\beta}}$ and the columns of matrix $\mathbf{C}$, respectively, the Hamiltonian can be constructed from its eigendecomposition as

$$\mathbf{H} = \mathbf{C}\mathrm{diag}(\tilde{\boldsymbol{\beta}})\mathbf{C}^{-1}. \tag{10}$$

Furthermore, the propagation constant $\bar{\beta}$ of an isolated waveguide can be used to compute matrix

$$\mathbf{T} = \mathbf{H} - \bar{\beta}\mathbf{I}, \tag{11}$$

whose elements are the coupling coefficients for the higher-order mode of interest. Here, $\mathbf{I}$ is the identity matrix.

By obtaining the matrix $\mathbf{T}$ numerically, using the method described above, we find that, for the low-crosstalk higher-order modes, $\mathbf{T}$ assumes the form of a heptadiagonal quasi-Toeplitz matrix with perturbed corners:

$$\mathbf{T} = \begin{bmatrix}
\delta_e & \kappa & \chi & \xi & & & & & \\
\kappa & \delta & \kappa & \chi & \xi & & & & \\
\chi & \kappa & \delta & \kappa & \chi & \xi & & & \\
\xi & \chi & \kappa & \delta & \kappa & \chi & \xi & & \\
 & \ddots & \ddots & \ddots & \ddots & \ddots & \ddots & \ddots & \\
 & & \xi & \chi & \kappa & \delta & \kappa & \chi & \xi \\
 & & & \xi & \chi & \kappa & \delta & \kappa & \chi \\
 & & & & \xi & \chi & \kappa & \delta & \kappa \\
 & & & & & \xi & \chi & \kappa & \delta_e.
\end{bmatrix}. \tag{12}$$

Here, the matrix elements that are not shown are equal to 0. The perturbation at the corners—specifically, a different self-coupling value δ_e for the edge waveguides—arises because these waveguides are adjacent to only one high-index core [43,44]. The coupling between the edge waveguides and their immediate neighbors also deviate slightly from other pairs of neighboring waveguides. However, this small deviation does not appear to have any noticeable effect for the AZ modes we consider and is therefore neglected. As mentioned earlier, the coupling κ to the neighboring waveguide can be made equal to zero by design. In such cases, the coupling to the second and third waveguides, described by coefficient χ and ξ, respectively, becomes the most pronounced origin of crosstalk. The coupling between more distant waveguides is found to be negligible, and hence, it is omitted from matrix $\mathbf{T}$.

Let us find the coupling coefficients for AZ modes in waveguide arrays like the one in Fig. 1, except that the waveguide height h is treated as a variable. The calculations are performed for an array of seven waveguides, but the results are independent of N. The coupling coefficients as a function of h are depicted in Fig. 2(a), showing κ crossing zero approximately at $h = 810$ nm. With $\kappa = 0$, the coupling coefficient χ describing the coupling to the second waveguides is dominant. This remains to be the case for waveguide heights in the range from 806 to 813 nm, which is wide compared to the subnanometer standard deviation feasible in Si waveguide fabrication [45]. The quantity $\Delta = \delta - \delta_e$ in Fig. 2(a) is the self-coupling mismatch between the edge and central waveguides. In this work, we use the AZ modes of Fig. 2(a) with h set to 810 nm as examples of low-crosstalk higher-order modes. The coupling coefficients of these modes are collected in Table I.

In general, direct coupling between neighboring waveguides can be canceled with various combinations of the waveguide height, width, and array period. This is shown in Fig. 2(b) that depicts κ at three different planes of the three-dimensional parameter space. Each of the planes has one constant parameter, which are $h = 850$ nm, $w = 550$ nm, and $\Lambda = 850$ nm. In order to ensure that the evanescent field of one waveguide is weak enough at the coordinates of the neighboring waveguide, not to violate Eq. (4), we have excluded waveguide arrays for which the gap between waveguides is smaller than $3/(f\gamma)$, where f is the confinement factor of the AZ mode and γ is the attenuation coefficient of the evanescent field (calculated from the norm of the electric field $\|\mathbf{E}(y)\| \exp(-\gamma(y)x)$ averaged over the waveguide

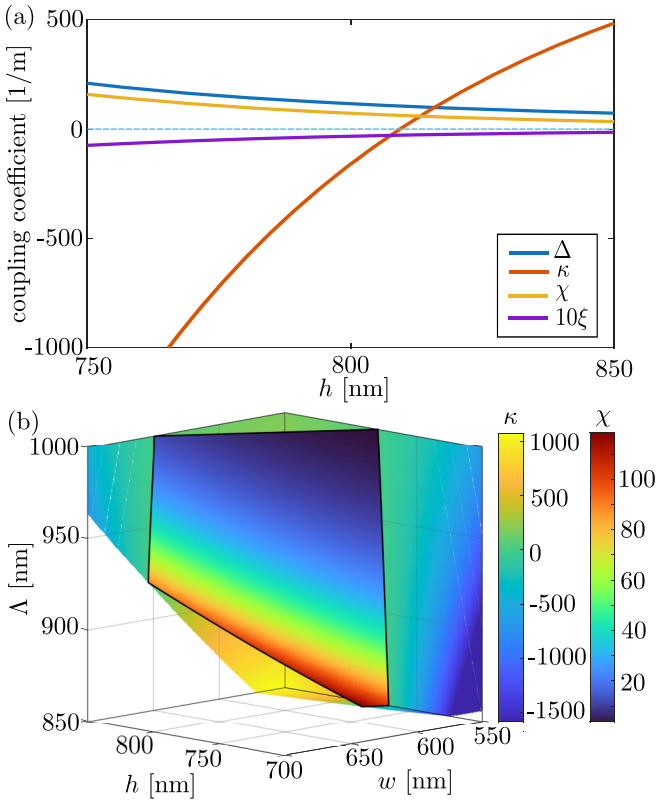


FIG. 2. (a) Relevant coupling coefficients as functions of waveguide height h for AZ modes. (b) The coupling coefficient κ as a function of two geometric parameters at planes $h = 850$ nm, $w = 550$ nm, and $\Lambda = 850$ nm, and the isosurface $\kappa = 0$ displaying the corresponding value of χ. The isosurface is outlined with a thicker black line.

height, with $y \in [0, h]$). Figure 2(b) includes an isosurface $\kappa = 0$ (outlined with a thicker black line), revealing that the suppression of κ primarily depends on the waveguide shape (the aspect ratio h/w); i.e., the optimal shape remains approximately the same regardless of the core size or the array period. Figure 2(b) also depicts the next coupling coefficient χ when κ is canceled, showing that the crosstalk can be reduced further by increasing the gap between the waveguides, as expected.

The ability of AZ modes to exhibit both positive and negative κ, or its complete vanishing, can be explained in a similar way as the crosstalk cancellation based on anisotropic metamaterial cladding [14], i.e., by separately examining how each Cartesian component of the electric field contributes to the coupling. For a pair of waveguides with a refractive index distribution $\tilde{n}(x, y)$, the coupling coefficient describing light transfer to the neighboring waveguide can be calculated as

$$\kappa = \frac{\omega\epsilon_0}{4} \iint_{-\infty}^{\infty} (\tilde{n}^2 - \bar{n}_1^2)\bar{\mathbf{e}}_1 \cdot \bar{\mathbf{e}}_2^* dxdy \tag{13}$$

or as half the difference between the propagation constants of the two supermodes, i.e., $\kappa = (\tilde{\beta}_1 - \tilde{\beta}_2)/2$ [7,46]. In Eq. (13), ω is the angular frequency of light, ϵ_0 the vacuum permittivity, and $\bar{n}_1(x, y)$ the refractive index distribution of the first waveguide. By expanding the dot product in Eq. (13), we can isolate the contribution of each electric field component to the overall coupling. These partial contributions are given by

$$\kappa_p = \frac{\omega\epsilon_0}{4} \iint_{-\infty}^{\infty} (\tilde{n}^2 - \bar{n}_1^2)\bar{e}_{1p}\bar{e}_{2p}^* dxdy \tag{14}$$

for $p \in \{x, y, z\}$. For example, Fig. 3(a) shows the coupling coefficient κ as a function of waveguide height, alongside the contributions from each Cartesian component of the field. Note that the antisymmetric supermode having a higher propagation constant than the symmetric one ($\tilde{\beta}_2 > \tilde{\beta}_1$) exhibits a negative coupling [23]. From Fig. 3(a), we see that the x component of the field induces a positive coupling, while the y and z components have negative contributions to the coupling coefficient. In low waveguides (with small h), the y component can easily prevail, rendering the coupling coefficient negative, but in tall waveguides, the y component is weak and the coupling coefficient is positive. Meanwhile, increasing the period (the gap between the waveguides) causes an exponential decrease in the strength of all the components of the coupling coefficient [see Fig. 3(b)], since at a larger distance, the waveguides "feel" weaker evanescent fields of each other. This makes the optimal size almost independent of the period. On the other hand, widening the waveguides decreases the gap, enhancing all the three components of κ, as shown in Fig. 3(c). However, the change in waveguide shape strengthens the y component further. Consequently, the optimal aspect ratio of the waveguides is almost constant, as seen also in Fig. 2(b). The negative contribution of the y component to the coupling can be understood by considering the transverse distribution of the electric-field vector in the coupled AZ modes. When the phases of these modes are equal, the y components of their electric-field vectors in the gap between the waveguides have opposite directions [see the white arrows in Fig. 3(d)]. This means that the evanescent field of the mode of one waveguide excites the mode in the other waveguide with a phase shift of π. This is in contrast with the x component, which points in the same direction in the gap and thereby promotes a positive, in-phase coupling.

TABLE I. Geometric parameters of the example waveguide array (with the values given in nm) and the corresponding coupling coefficients (in m^{-1}) for AZ modes with suppressed direct coupling between neighboring waveguides.

h	w	Λ	δ	δ_e	κ	χ	ξ
810	600	900	181	78	6	61	−3

III. ANALYSIS OF HIGHER-ORDER SUPERMODES IN THE CROSSTALK SUPPRESSION REGIME

In general, the ways in which the higher-order and fundamental supermodes distribute light among the waveguides can differ significantly (cf. Fig. 1 to the corresponding figures in Refs. [39,47]). Most notably, the higher-order supermodes can concentrate the light at the edges of the array, as is the case for the third and fourth supermodes in Fig. 1. In this section, we investigate into the origins of these peculiarities. The unconventional dynamics of the higher-order modes is discussed in the next section.

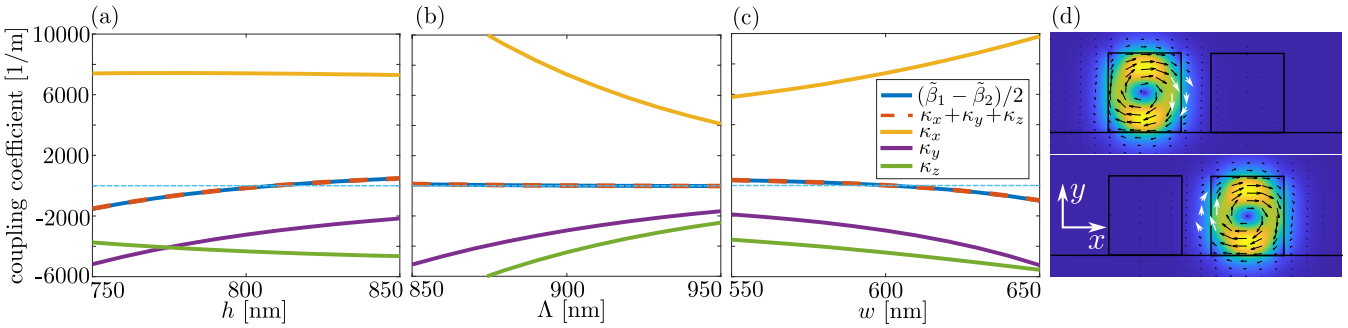


FIG. 3. Coupling coefficient κ and its components originating from the Cartesian components of the electric field as functions of (a) waveguide height, (b) period, and (c) width calculated for a pair of waveguides. The constant parameters are $h = 810$ nm, $w = 600$ nm, and $\Lambda = 900$ nm. (d) The transverse electric field distributions of AZ modes guided by individual waveguides highlighting their opposite y components of the evanescent fields in the gap between the waveguides (white arrows). The coupling takes place via these components.

In the previous section, we found the higher-order supermodes numerically to construct the corresponding Hamiltonian. This allowed us to show that matrices **H** and **T** have the form of a heptadiagonal quasi-Toeplitz matrix with perturbed corners. With this insight, we now reverse the analysis and search for the eigenvalues and eigenvectors of these matrices analytically. Notice that the matrix **T** has the same eigenvectors as **H**, while its mth eigenvalue τ_m satisfies the equality $\tilde{\beta}_m = \bar{\beta} + \tau_m$, because

$$\mathrm{diag}(\tilde{\boldsymbol{\beta}}) = \mathbf{C}^{-1}\tilde{\mathbf{H}}\mathbf{C} = \bar{\beta}\mathbf{I} + \mathbf{C}^{-1}\mathbf{T}\mathbf{C}. \tag{15}$$

Thus, solving the eigenproblem for matrix **T** reveals the dependence of the supermodes on the coupling coefficients, which is the topic of this section.

It has been recently shown that, for matrices of the form given in Eq. (12), the eigenvalues τ_m satisfy a certain set of equations (see Eqs. (2.7), (2.9), (2.11), and (2.13) in Ref. [34], and Eqs. (3.4b)–(3.7b) in Ref. [35]), which can be combined into a single expression:

$$\mathbf{s}_1^T[\mathbf{u}(\tau_m) \circ \mathbf{s}_1] = 1, \tag{16}$$

where $\circ$ denotes the Hadamard product, $\mathbf{s}_1$ is the first column of the discrete sine transformation matrix of type 1 (**S**), the elements of which have the form $s_{lm}=\sqrt{2/(N+1)}\sin m\phi_l$, where $\phi_l = l\pi/(N+1)$. The vector **u** in Eq. (16) is given by

$$\mathbf{u}(\tau_m) = 2\left[\frac{\chi-\Delta+4\xi\cos\phi_1}{\tau_m-\nu(\phi_1)}\ 0\ \frac{\chi-\Delta+4\xi\cos\phi_3}{\tau_m-\nu(\phi_3)}\ 0\cdots\right]^T, \tag{17}$$

if m is odd, and by

$$\mathbf{u}(\tau_m) = 2\left[0\ \frac{\chi-\Delta+4\xi\cos\phi_2}{\tau_m-\nu(\phi_2)}\ 0\ \frac{\chi-\Delta+4\xi\cos\phi_4}{\tau_m-\nu(\phi_4)}\cdots\right]^T, \tag{18}$$

if m is even. Here,

$$\nu(\phi) = \delta + 2(\kappa\cos\phi + \chi\cos 2\phi + \xi\cos 3\phi) \tag{19}$$

is the symbol of the corresponding heptadiagonal Toeplitz matrix (i.e., matrix **T** without the corner perturbations). The eigenvalues τ_m obtained from Eq. (16) accurately describe the propagation constants of the AZ supermodes, as demonstrated in Fig. 4. The waveguide parameters used are given in Table I. The circles in Fig. 4 depict the eigenvalues $\tau_m = \tilde{\beta}_m - \bar{\beta}$ obtained using COMSOL Multiphysics for an array of 20 waveguides, while the crosses denote the corresponding eigenvalues calculated by solving Eq. (16) via a root-finding algorithm. The blue solid line in Fig. 4 shows the eigenvalues of matrix **T** when its size is taken to the asymptotic limit of $N \to \infty$. For the unperturbed Toeplitz matrix, the asymptotic limit of the eigenvalues is given by its symbol $\nu(\phi)$ [48,49]. Indeed, from Eq. (19) we can see that, when $\chi \gg \{\kappa, \xi\}$, $\tau_m = \nu(\phi_m)$ yields the U-shaped curve shown in Fig. 4. Note also that, in an infinite (edgeless) waveguide array, the Bloch waves of the form $\bar{a}_n(\phi) = a_0 \exp i(\tilde{\beta}(\phi)z + \phi n)$ satisfy the corresponding dispersion relation $\tilde{\beta}(\phi) = \bar{\beta} + \nu(\phi)$, where ϕ is the spatial frequency of the Bloch wave, i.e., the phase shift between adjacent waveguides [24,25]. This highlights the usefulness of the higher-order modes not only in suppression of crosstalk, but also in engineering the dispersion curve $\tilde{\beta}(\phi)$ for other purposes through tuning the waveguide coupling coefficients.

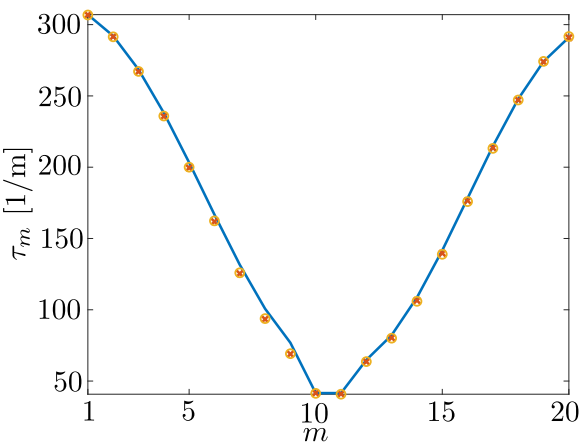


FIG. 4. Eigenvalues of matrix **T** corresponding to an array of 20 waveguides guiding AZ modes, for which the parameters are given in Table I.

Taking into account the perturbed corners of matrix **T**, we find that two of its eigenvalues break the pattern given by $\nu(\phi)$ [35,50], as can be seen to be the case in Fig. 4 for $m = 10$ and $m = 11$. The two special eigenvalues, known as boundary-condition-dependent eigenvalues, can be computed using the procedure described in Ref. [50]. In order to find the closed-form expressions for these eigenvalues, we assume that ξ is negligible. This yields (see Appendix)

$$\tau_{\mathrm{b}} = \delta_{\mathrm{e}} - \frac{\chi^2}{\Delta} - \frac{\Delta\kappa^2}{(\Delta+\chi)^2} \tag{20}$$

for both eigenvalues τ_{b}, meaning that the corresponding supermodes are degenerate. Figure 4 shows that the eigenvalues given by Eq. (20) (blue line between $m = 10$ and $m = 11$) are in good agreement with the propagation constants obtained using FEM. The procedure in Ref. [50] also explains when the boundary-condition-dependent supermodes exist. In Appendix, we show that such supermodes appear in waveguide arrays whose coupling coefficients satisfy the following inequalities:

$$|\kappa| < 2(\Delta+\chi)\sqrt{\frac{\chi}{\Delta}} \tag{21}$$

and

$$0 < \chi < \Delta, \tag{22}$$

showing that the coupling to the first neighboring waveguide needs to be suppressed. Additionally, a positive coupling to the second neighboring waveguides needs to be weaker than the self-coupling mismatch between the edge and inner waveguides.

Like the eigenvalues, the eigenvectors of heptadiagonal quasi-Toeplitz matrices with perturbed corners were found in Refs. [34,35]. This result allows us to express the eigenvectors of **T** (columns of matrix **C**) using a matrix product

$$\mathbf{C} = \mathbf{S}\mathbf{V}, \tag{23}$$

where matrix **V** is formed by column vectors $\mathbf{v}_m$ given by

$$\mathbf{v}_m = \frac{\mathbf{u}(\tau_m)\circ\mathbf{s}_1}{\sqrt{\mathbf{s}_1^T[\mathbf{u}(\tau_m)^{\circ 2}\circ\mathbf{s}_1]}}. \tag{24}$$

Here, $\mathbf{u}^{\circ 2} = \mathbf{u}\circ\mathbf{u}$. Considering the asymptotic limit, we find from Eqs. (17) and (18) that the mth element of $\mathbf{u}(\tau_m)$ diverges, since $\lim_{N\to\infty}\tau_m = \nu(\phi_m)$. Consequently, the lth element of the vector $\mathbf{v}_m$ is given by the Kronecker delta, $\lim_{N\to\infty} v_{lm} = \delta_{lm}$, turning matrix **V** into the identity matrix, except for the columns corresponding to the boundary-condition-dependent eigenvectors. This makes the mth eigenvector $\mathbf{c}_m$ approximately equal to the mth column vector of the discrete sine transformation matrix $\mathbf{s}_m$. This asymptotic behavior aligns with the conventional form of supermodes observed when κ is large [39,47]. In fact, the transformation in Eq. (8) can be decomposed as follows:

$$\tilde{\mathbf{a}} = \mathbf{V}^T\mathbf{S}\bar{\mathbf{a}}, \tag{25}$$

where the multiplication by matrix **S** expresses the field in terms of conventional supermodes, whereas the matrix **V** transforms the supermodes to their unconventional form. Therefore, the suppression of κ may lead to supermodes with nonstandard eigenvectors only if the number of waveguides is sufficiently small or if the supermodes are boundary condition dependent. Moreover, the symmetry of the supermodes with odd m and the antisymmetry of the supermodes with even m are always preserved, thanks to the zero elements in Eqs. (17) and (18).

To determine the asymptotic form of the boundary-condition-dependent eigenvectors of matrix **T**, we again follow the procedure outlined in Ref. [50]. If $\xi = 0$, we find that the nth element of the eigenvector $\mathbf{c}_m^{\mathrm{b}}$ (with "b" standing for the "boundary-condition-dependent") has the form (see Appendix)

$$c_{nm}^{\mathrm{b}} = \mathcal{N}\left\{\left(\frac{\chi}{\Delta}\right)^{n/2}\sin(n\varphi) \pm \left(\frac{\chi}{\Delta}\right)^{(N+1-n)/2}\sin[(N+1-n)\varphi]\right\}, \tag{26}$$

where the sign in front of the second term is positive for odd m and negative for even m, making the respective supermodes symmetric and antisymmetric. Here, the coupling coefficients are assumed to be such that the two eigenvectors exist, i.e., they satisfy Eqs. (21) and (22). In Eq. (26), $\mathcal{N}$ is a normalization coefficient ensuring that $\|\mathbf{c}_m^{\mathrm{b}}\| = 1$ and φ is given by the expression

$$\varphi = \begin{cases} \pi - \arctan\sqrt{\varkappa^{-2}-1}, & \kappa > 0, \\ \arctan\sqrt{\varkappa^{-2}-1}, & \kappa < 0, \end{cases} \tag{27}$$

where we have introduced a variable

$$\varkappa = \frac{\kappa}{2(\Delta+\chi)}\sqrt{\frac{\Delta}{\chi}} \tag{28}$$

that takes values between -1 and 1 [see Eq. (21)]. For small values of $|\kappa|$, Eq. (27) yields $\varphi \approx \pi/2$, making every second waveguide dark. This makes the propagation constants highly dependent on χ, yielding exceptionally low τ_b for $\chi > 0$. In addition, since we have $\sqrt{\chi/\Delta} < 1$, Eq. (26) shows that the field of the boundary-condition-dependent supermodes is concentrated at the edges of the waveguide array, and more so if Δ is large compared to χ. This further lowers the values of propagation constants, owing to the low self-coupling of the edge waveguides [see Eq. (20)]. However, when $\chi = \Delta$, the field is no longer concentrated at the edges of the array, and the boundary-condition-dependent supermodes cease to exist.

In order to verify the correctness of Eq. (23), the solutions are compared to those obtained by numerically solving the Helmholtz equation for an array of 20 waveguides with the parameter values given in Table I. The eigenvectors of the AZ supermodes obtained using the two approaches, represented as rows of matrix $\mathbf{C}^T$, are depicted in Figs. 5(a) and 5(b). The matrices shown in the figure describe the supermode field distributions in the same way as the matrix in Fig. 1. They are in good agreement with each other, having a mean 2-norm error $\sum_{m=1}^{N}\|\mathbf{c}_m^{\mathrm{ana}} - \mathbf{c}_m^{\mathrm{num}}\|/N = 0.08$. Furthermore, the eigenvectors resemble the solutions corresponding to the asymptotic limit shown in Fig. 5(c), including the boundary-condition-dependent supermodes that have the optical power concentrated at the edges of the array. This is as expected, given that the eigenvalues shown in Fig. 4

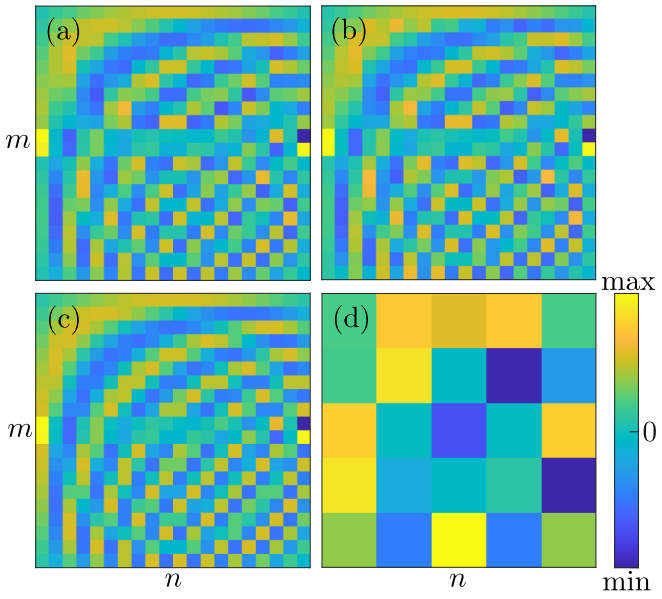


FIG. 5. Matrix $\mathbf{C}^T$ for AZ modes in an array of 20 waveguides found by (a) numerically solving Eq. (3), (b) using Eq. (23) and the coupling coefficients from Table I, and (c) considering the asymptotic limit, i.e., $\mathbf{C}^T = \mathbf{S}$, except for the rows 10 and 11 whose elements are given by Eq. (26). (d) The corresponding matrix for an array of five waveguides calculated using Eq. (23). The depicted matrices represent the corresponding supermode field distributions similarly to the distribution in Fig. 1.

were close to their asymptotic values too. However, if the number of waveguides is significantly reduced, e.g., to five, the supermodes corresponding to the coupling coefficients in Table I show significant deviation from the conventional form, as can be seen from Fig. 5(d). The matrix $\mathbf{C}^T$ in Fig. 5(d), obtained using Eq. (23), also agrees with the FEM solution (see Fig. 1).

IV. PROPAGATION OF LOW-CROSSTALK HIGHER-ORDER MODES

Once the eigenvalues and eigenvectors of the Hamiltonian $\mathbf{H}$ are known, propagation of light in the array, also known as discrete diffraction, can be modeled using Eq. (7). For instance, when an AZ mode is launched into the central waveguide of an array defined in Table I, optical power $|\bar{a}_n(z)|^2$ spreads upon propagation, as shown in Fig. 6(a). The tendency of light to skip every second waveguide is observed. This can be explained in terms of supermodes, noting that the light in the tenth waveguide excites mth and $(N+1-m)$th supermodes with equal amplitudes but opposite phases (see the tenth column of $\mathbf{C}^T$ in Fig. 5). These supermodes interfere destructively in every odd waveguide (see the rows of $\mathbf{C}^T$ in Fig. 5). Furthermore, as these pairs of supermodes are nearly degenerate (see Fig. 4), the destructive interference is maintained throughout the propagation. Indeed, the impulse response of an infinite (edgeless) waveguide array excited at the lth waveguide is given by [25,28,51]

$$\begin{aligned}\bar{a}_n(z) &= \bar{a}_l(0)\exp[i(\bar{\beta}+\delta)z]i^{(n-l)} \\ &\quad\times\sum_{q=-\infty}^{\infty}\sum_{p=-\infty}^{\infty}(-i)^p(-1)^q J_{n-l-2p-3q}(2\kappa z) \\ &\quad\times J_p(2\chi z)J_q(2\xi z) \\ &= \bar{a}_l(0)\exp[i(\bar{\beta}+\delta)z]i^{(n-l)}J_{n-l}(2\kappa z, 2\chi z, 2\xi z; -\mathrm{i}, -1),\end{aligned} \tag{29}$$

where $J_\nu(\cdot,\cdot,\cdot;\cdot,\cdot)$ is the generalized Bessel function of three variables and two parameters. From Eq. (29), we can see that

$$J_{n-l}(0, 2\chi z, 0; -i, -1) = \begin{cases}(-i)^{(n-l)/2}J_{(n-l)/2}(2\chi z), & \text{if } (n-l)/2 \in \mathbb{Z}, \\ 0, & \text{otherwise.}\end{cases} \tag{30}$$

Hence, when $|\chi| \gg |\kappa|$ (and $|\chi| \gg |\xi|$), the crosstalk dynamics is qualitatively similar to that exhibited by the fundamental modes (for which $\bar{a}_n(z) \propto J_{n-l}(2\kappa z)$ [52,53]), except for every second waveguide remaining dark. In Fig. 6(a), the propagation distance considered is $z = 5/|\chi| = 81$ mm. The impulse response of the fundamental mode TE_{00} in the same waveguide array is shown in Fig. 6(b). The considered propagation distance, however, is much shorter being equal to $z = 10/|\kappa| = 9.2$ mm. As expected, the fundamental mode spreads without missing every second waveguide and at a much faster rate ($\kappa = 1086\,\mathrm{m}^{-1}$). From Fig. 2(a), we see that the height of the waveguide would need to deviate approxi-

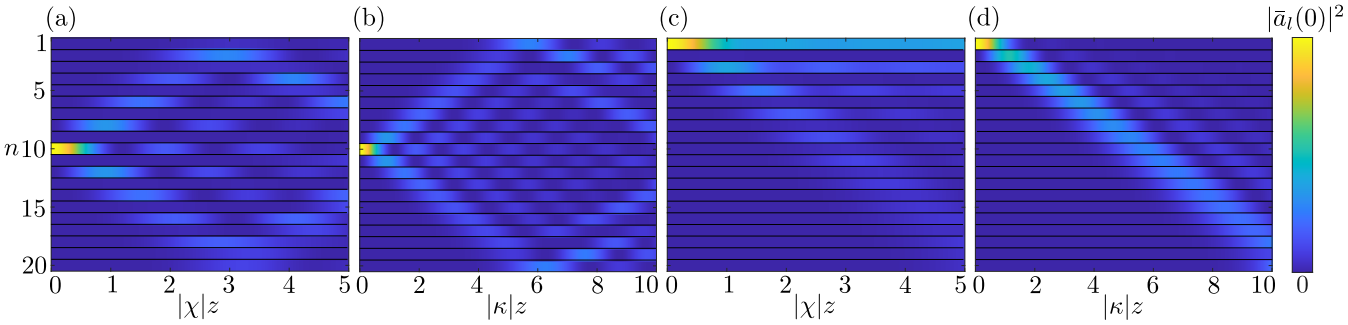


FIG. 6. The optical power of [panels (a) and (c)] higher-order and [panels (b) and (d)] fundamental modes propagating in an array of 20 waveguides. In panels (a) and (b), light is originally confined in the tenth waveguide, while in panels (c) and (d), in the first waveguide of the array. Note that the horizontal segments into which the plots are divided are not the actual waveguides.

mately by 40 nm from the ideal case before reaching the same level of crosstalk as the fundamental mode ($\kappa = -1000$ m^{-1} for $h = 770$ nm), demonstrating the crosstalk suppression resistance to fabrication errors. In principle, scattering of the AZ mode on fabrication imperfections can lead to some power conversion to the fundamental mode, which is prompt to crosstalk. However, such a process is expected to be insignificant due to the orthogonality of the modes. It is more likely that the scattered light will simply be radiated away from the system.

If the AZ mode is launched into an edge waveguide instead of the central one, a large portion of the optical power gets trapped there, as shown in Fig. 6(c). This effect is similar to light trapping in so-called defect edge waveguides [30]. Here, however, the edge waveguides are the same as all the other waveguides, but their self-coupling coefficients are lower. The confinement of light in the edge waveguide originates from the excitation of two boundary-condition-dependent supermodes. In contrast to AZ modes, the fundamental modes do not satisfy Eq. (21) and therefore do not support boundary-condition-dependent supermodes, allowing the light to leak out from the edge waveguide, as shown in Fig. 6(d).

In addition to suppressing crosstalk, higher-order modes provide a platform for realizing other intriguing discrete diffraction phenomena, such as self-collimation. In an infinite waveguide array, a sufficiently broad discrete beam of light composed of Bloch waves with center spatial frequency ϕ_c is self-collimated, if $\partial^2\tilde{\beta}/\partial\phi^2|_{\phi=\phi_c} = 0$ [25,31,32]. A Bloch wave with spatial frequency ϕ propagates at an angle $\theta = \arctan(\phi/\tilde{\beta}\Lambda)$ with respect to the z axis. When the long-distance coupling is negligible, self-collimation can only occur at $\phi_c = \pi/2$, leading to a tilted beam trajectory [31]. More generally, the coupling coefficients can be combined to obtain self-collimation for arbitrary ϕ_c, including $\phi_c = 0$ when $\kappa = -4\chi$ [25]. Such coupling coefficients could be realized using higher-order modes, e.g., with AZ modes in a waveguide array with $h = 780$ nm, $w = 590$ nm, and $\Lambda = 880$ nm. We find that the self-collimation can be improved by setting ϕ_c to a small nonzero value, say $\pi/10$, satisfying the condition $\kappa \approx -10/3\chi$. For AZ modes, the condition is met with parameters $h = 850$ nm, $w = 660$ nm, and $\Lambda = 1000$ nm, which completely flattens the dispersion curve for low spatial frequencies ϕ, except for a small distortion caused by the boundary-condition-dependent eigenvalues at $\varphi = 0.18\pi$, as shown in Fig. 7(a). In both examples, the gap between the waveguides is larger than $3/(f\gamma)$ and the supermodes conform to Eq. (4). Thanks to the flat dispersion curve, a sufficiently broad discrete Gaussian beam, corresponding to the initial condition

$$\bar{a}_n(0) = a_0 \exp\left[-\left(\frac{n - N/2}{w_G}\right)^2\right] \tag{31}$$

can propagate through the array without any spreading. This is demonstrated in Fig. 7(b) for a beam of width $w_G = 4$, showing propagation over a large distance $z = 20/|\kappa| = 348$ mm. Note that the lack of broadening is not due to the crosstalk suppression, but due to the interplay of the coupling of light to the first and more distant second neighboring

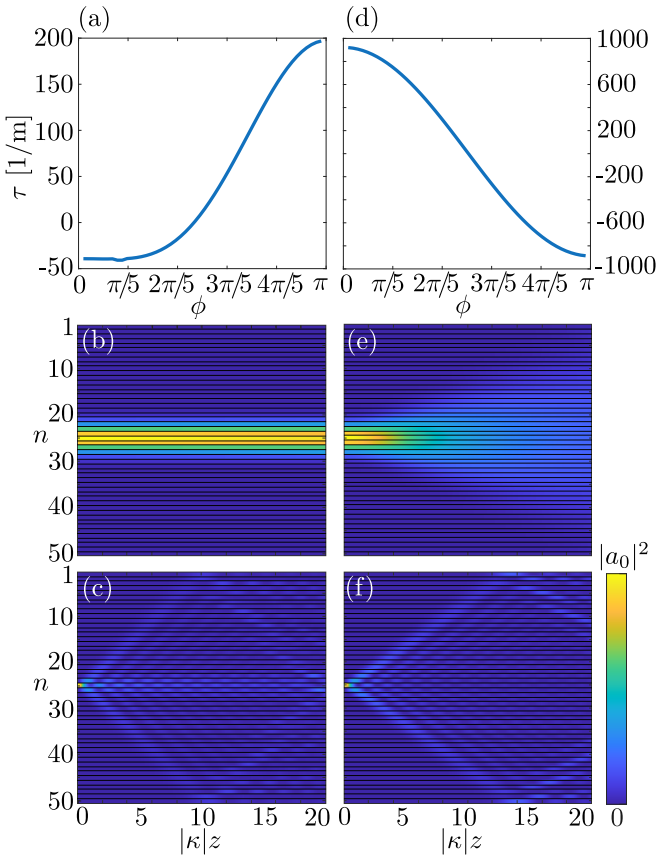


FIG. 7. Dispersion curves $\tilde{\beta}(\phi) = \bar{\beta} + \tau(\phi)$ of (a) higher-order and (d) fundamental modes. The discrete Gaussian beams composed of these modes are shown in panels (b) and (e), respectively. The impulse responses of the array are, respectively, shown in panels (c) and (f).

waveguides, as evident from the impulse response shown in Fig. 7(c). The Gaussian beam consists of sufficiently low-frequency supermodes, which are degenerate [see Fig. 7(a)]. This prevents the beam from broadening. For comparison, the propagation of a discrete Gaussian beam composed of fundamental modes [see the dispersion curve in Fig. 7(d)] is shown in Fig. 7(e). It spreads significantly when propagating over a much shorter distance of $20/|\kappa| = 44$ mm. The impulse response for the fundamental input mode is shown in Fig. 7(f). We see that the beam spreading rate is reduced in the case of AZ modes by at least two orders of magnitude.

To find the parameters of a waveguide array capable of self-collimation, we have calculated the coupling coefficients as functions of these parameters, as described in Sec. II. However, this task is computationally demanding. To accelerate the dispersion engineering process, the procedure for computing the coupling coefficients could be used in tandem with a certain optimization algorithm (such as simulated annealing) to seek for the desired dispersion characteristics. This can become crucial if the design space is expanded with additional degrees of freedom, e.g., by considering trapezoidal waveguides.

V. CONCLUSIONS

In this work, the unique properties of low-crosstalk higher-order modes were investigated in terms of the coupled-mode theory. We have shown how the long-range coupling coefficients of higher-order modes can be extracted from numerically computed supermodes. Focusing on AZ modes guided by Si waveguides on a glass substrate, we demonstrated that the coupling between neighboring waveguides can be positive, negative, or absent. In the third case, the long-range coupling becomes dominant. The crosstalk suppression between neighboring waveguides was explained by separately examining the vector components of the electric field and their contributions to the coupling. In addition to the overall crosstalk reduction, the unconventional combinations of the coupling coefficients exhibited by the higher-order modes have been recognized to be of importance in view of more fundamental studies of the discrete diffraction phenomenon. The described computational tools are general and can easily be applied to different higher-order modes, wavelengths, and waveguide arrays. Of particular interest would be the realization of a waveguide array in which both the short- and long-range coupling are simultaneously suppressed, resulting in an exceptionally low crosstalk.

We have also analyzed the dependence of higher-order supermodes on the coupling coefficients and investigated deeper into the discrete diffraction phenomenon. We showed that the higher-order supermodes can have different field distributions than the fundamentals modes, especially if the number of waveguides is small. We have also explained how the low self-coupling of the edge waveguides in the array can give rise to boundary-condition-dependent supermodes, which leads to light trapping in the edge waveguides. Finally, we have demonstrated the discrete self-collimation effect enabled by higher-order modes. We believe that this effect can be of interest in view of on-chip optical information processing, as it introduces an alternative way to prevent optical information transferred in a waveguide array from transverse spreading. We also believe that combining the unconventional coupling characteristics of higher-order modes with nonlinear effects in optical waveguides that, in addition, can be spatially modulated represents an interesting direction for future research and applications.

ACKNOWLEDGMENTS

This work is part of the Research Council of Finland Flagship Programme, Photonics Research and Innovation (PREIN), decision number 346529. The calculations presented above were performed using computer resources within the Aalto University School of Science "Science-IT" project.

DATA AVAILABILITY

The data that support the findings of this article are not publicly available upon publication because it is not technically feasible and/or the cost of preparing, depositing, and hosting the data would be prohibitive within the terms of this research project. The data are available from the authors upon reasonable request.

APPENDIX: BOUNDARY-CONDITION-DEPENDENT EIGENVALUES AND EIGENVECTORS IN THE ASYMPTOTIC LIMIT

The derivation of the boundary-condition-dependent eigenvalues and eigenvectors of matrix $\mathbf{T}$ in the asymptotic limit follows the procedure outlined in Algorithm 4.2 of Ref. [50]. To ensure analytical tractability, we set $\xi = 0$, which is a simplification whose necessity will become clear later. This simplification introduces a small (usually negligible) error to the description of higher-order modes of interest, but offers valuable insight into the topic.

Setting ξ to 0 reduces $\mathbf{T}$ to a pentadiagonal matrix. With this in mind, we start by assuming that the elements of the eigenvector $\mathbf{c}$ can be written in the form

$$c_n = \alpha_1 \psi_1^n + \alpha_2 \psi_2^n, \tag{A1}$$

where α_1, α_2, ψ_1, and ψ_2 are unknown complex numbers to be determined. In the asymptotic limit, an eigenvector may depend on either the left or the right boundary condition. For example, the eigenvector depending on the left-boundary condition, $\mathbf{c}_{\text{left}}$, satisfies the equation

$$\begin{bmatrix} \delta_e & \kappa & \chi & 0 \\ \kappa & \delta & \kappa & \chi \end{bmatrix} \begin{bmatrix} \alpha_1\psi_1 + \alpha_2\psi_2 \\ \alpha_1\psi_1^2 + \alpha_2\psi_2^2 \\ \alpha_1\psi_1^3 + \alpha_2\psi_2^3 \\ \alpha_1\psi_1^4 + \alpha_2\psi_2^4 \end{bmatrix} = \tau_b \begin{bmatrix} \alpha_1\psi_1 + \alpha_2\psi_2 \\ \alpha_1\psi_1^2 + \alpha_2\psi_2^2 \end{bmatrix}, \tag{A2}$$

where τ_b is the corresponding eigenvalue. The left-hand side of Eq. (A2) can be recognized as the product of the 2×4 matrix block, taken from the top left corner of $\mathbf{T}$, and the first four elements of the eigenvector $\mathbf{c}_{\text{left}}$. In addition to solving Eq. (A2), the complex numbers ψ_1 and ψ_2 have to correspond to the same eigenvalue τ_b, making them the roots of the following fourth-degree polynomial:

$$[\chi \quad \kappa \quad \delta \quad \kappa \quad \chi] \begin{bmatrix} \psi_j^{l-2} \\ \psi_j^{l-1} \\ \psi_j^{l} \\ \psi_j^{l+1} \\ \psi_j^{l+2} \end{bmatrix} = \tau_b \psi_j^l$$

$$\Rightarrow \chi\left(\psi_j^4 + 1\right) + \kappa\left(\psi_j^3 + \psi_j\right) - \tau_b \psi_j^2 = 0 \tag{A3}$$

obtained by taking the product of the lth row vector of $\mathbf{T}$ with vector $\boldsymbol{\psi}_j = [\psi_j^1 \ \psi_j^2 \ \cdots \ \psi_j^N]^T$ for both $j = 1$ and $j = 2$. This gives us a system of four equations, which has four solutions, two of which are trivial ($\mathbf{c}_{\text{left}} = 0$). The two remaining solutions are identical and given by

$$\tau_b = \delta_e - \frac{\chi^2}{\Delta} - \frac{\Delta\kappa^2}{(\Delta + \chi)^2}, \tag{A4}$$

$$\psi_1 = \frac{-\Delta\kappa + i\sqrt{\Delta[4\chi(\Delta + \chi)^2 - \Delta\kappa^2]}}{2\Delta(\Delta + \chi)}, \tag{A5}$$

$$\psi_2 = \psi_1^*, \tag{A6}$$

$$\alpha_1 = -\alpha_2. \tag{A7}$$

Note that this solution also becomes trivial if $\psi_1 = \psi_2$, which occurs when

$$4\chi(\Delta + \chi)^2 - \Delta\kappa^2 < 0, \tag{A8}$$

or more insightfully, if

$$\chi < 0 \quad \text{or} \quad |\kappa| > 2(\Delta + \chi)\sqrt{\frac{\chi}{\Delta}}. \tag{A9}$$

Additionally, Ref. [50] establishes one more condition that the solution has to satisfy in order to correspond to a boundary-condition-dependent eigenvalue/eigenvector, namely, that $|\psi_1| = |\psi_2|$ has to obey the inequality

$$|\psi_2| < |\psi_3|, \tag{A10}$$

where $|\psi_3| = |\psi_4|$ is the absolute value of the other complex conjugate pair of the roots that solve Eq. (A3) for the eigenvalue given by Eq. (A4). These roots are given by

$$\psi_3 = \frac{-\Delta\kappa + i\sqrt{\Delta[4\chi(\Delta + \chi)^2 - \Delta\kappa^2]}}{2\chi(\Delta + \chi)}, \tag{A11}$$

$$\psi_4 = \psi_3^*. \tag{A12}$$

Comparing the denominators in Eqs. (A5) and (A11), we see that the condition holds when

$$\Delta > \chi. \tag{A13}$$

It is worth noting that, if coefficients $\xi \neq 0$ were included in matrix $\mathbf{T}$, we would end up with a system of equations involving sixth-degree polynomials, rendering the problem analytically intractable.

The eigenvalue and eigenvector associated with the right boundary condition can be obtained by applying the procedure described earlier to the flipped matrix $\mathbf{FTF}$. Here, $\mathbf{F}$ denotes the $N \times N$ exchange matrix:

$$\mathbf{F} = \begin{bmatrix} & & & 1 \\ & & 1 & \\ & \iddots & & \\ 1 & & & \end{bmatrix}. \tag{A14}$$

That said, the flipped matrix is identical to $\mathbf{T}$ itself, due to its bisymmetry. Consequently, the left- and right-boundary-condition-dependent eigenvalues of $\mathbf{T}$ are equal, whereas

$$\begin{aligned} \mathbf{c}_{\text{right}} &= \mathbf{F}\mathbf{c}_{\text{left}} \\ \Rightarrow c_n^{\text{right}} &= c_{N+1-n}^{\text{left}}. \end{aligned} \tag{A15}$$

Clearly, the existence of right-boundary-condition-dependent supermode hinges on exactly the same conditions as its left counterpart.

Since the left- and right-boundary-condition-dependent eigenvalues are degenerate in the asymptotic limit, the eigenvectors can also be written as

$$\mathbf{c}_{\text{odd}} = \mathbf{c}_{\text{left}} + \mathbf{c}_{\text{right}}, \tag{A16}$$

$$\mathbf{c}_{\text{even}} = \mathbf{c}_{\text{left}} - \mathbf{c}_{\text{right}}, \tag{A17}$$

following the distributive property of the matrix multiplication:

$$\mathbf{T}(\mathbf{c}_{\text{right}} + \mathbf{c}_{\text{left}}) = \tau_{\text{b}}(\mathbf{c}_{\text{right}} + \mathbf{c}_{\text{left}}), \tag{A18}$$

$$\mathbf{T}(\mathbf{c}_{\text{right}} - \mathbf{c}_{\text{left}}) = \tau_{\text{b}}(\mathbf{c}_{\text{right}} - \mathbf{c}_{\text{left}}). \tag{A19}$$

Indeed, it appears that the boundary-condition-dependent eigenvectors found by solving Eqs. (3) and (23) for a finite number of waveguides resemble $\mathbf{c}_{\text{odd}}$ and $\mathbf{c}_{\text{even}}$ rather than $\mathbf{c}_{\text{left}}$ and $\mathbf{c}_{\text{right}}$. Here, the subscripts "even" and "odd" refer to the parity of the eigenvector index m. It should be noted that, since the supermodes are nearly degenerate, numerical confirmation of this result may require extremely fine mesh when solving Eq. (3) via FEM, particularly for large waveguide arrays.

In order to gain more insight into the properties of the eigenvectors $\mathbf{c}_{\text{odd}}$ and $\mathbf{c}_{\text{even}}$, it is convenient to write $\psi = \psi_1 \in \mathbb{C}$ in the polar form. Assuming that the coupling coefficients are such that the boundary-condition-dependent supermodes exist, we have

$$\psi = \sqrt{\frac{\chi}{\Delta}} \exp \mathrm{i}\varphi, \tag{A20}$$

where φ is given by the following two-argument arctangent:

$$\varphi = \arctan2(\sqrt{\Delta[4\chi(\Delta + \chi)^2 - \Delta\kappa^2]}, -\Delta\kappa). \tag{A21}$$

By introducing a parameter $\varkappa \in [-1, 1]$ defined as

$$\varkappa = \frac{\kappa}{2(\Delta + \chi)}\sqrt{\frac{\Delta}{\chi}}, \tag{A22}$$

we obtain

$$\varphi = \begin{cases} \pi - \arctan\sqrt{\varkappa^{-2} - 1}, & \kappa > 0, \\ \arctan\sqrt{\varkappa^{-2} - 1}, & \kappa < 0. \end{cases} \tag{A23}$$

Using the polar form of ψ, we find that

$$\begin{aligned} c_n^{\text{odd}} &= \alpha_2(\psi^{*n} - \psi^n + \psi^{*N+1-n} - \psi^{N+1-n}) \\ &= 2i\alpha_2\left\{\left(\frac{\chi}{\Delta}\right)^{n/2} \sin(n\varphi) \right. \\ &\quad \left. + \left(\frac{\chi}{\Delta}\right)^{(N+1-n)/2} \sin[(N+1-n)\varphi]\right\}. \end{aligned} \tag{A24}$$

With $\alpha_2 = -i\mathcal{N}/2$, we obtain

$$\begin{aligned} c_n^{\text{odd}} &= \mathcal{N}\left\{\left(\frac{\chi}{\Delta}\right)^{n/2} \sin(n\varphi) \right. \\ &\quad \left. + \left(\frac{\chi}{\Delta}\right)^{(N+1-n)/2} \sin[(N+1-n)\varphi]\right\}, \end{aligned} \tag{A25}$$

where $\mathcal{N} \in \mathbb{R}$ normalizes $\mathbf{c}_{\text{odd}}$ such that $\|\mathbf{c}_{\text{odd}}\| = 1$. The corresponding expression for $\mathbf{c}_{\text{even}}$ can be found analogously.

[1] D. Thomson, A. Zilkie, J. E. Bowers, T. Komljenovic, G. T. Reed, L. Vivien, D. Marris-Morini, E. Cassan, L. Virot, J.-M. Fédéli, J.-M. Hartmann, J. H. Schmid, D.-X. Xu, F. Boeuf, P. O'Brien, G. Z. Mashanovich, and M. Nedeljkovic, Roadmap on silicon photonics, J. Opt. **18**, 073003 (2016).

[2] W. Bogaerts and L. Chrostowski, Silicon photonics circuit design: Methods, tools and challenges, Laser Photon. Rev. **12**, 1700237 (2018).

[3] N. Margalit, C. Xiang, S. M. Bowers, A. Bjorlin, R. Blum, and J. E. Bowers, Perspective on the future of silicon photonics and electronics, Appl. Phys. Lett. **118**, 220501 (2021).

[4] N. Izhaky, M. T. Morse, S. Koehl, O. Cohen, D. Rubin, A. Barkai, G. Sarid, R. Cohen, and M. J. Paniccia, Development of CMOS-compatible integrated silicon photonics devices, IEEE J. Sel. Top. Quantum Electron. **12**, 1688 (2006).

[5] A. H. Atabaki, S. Moazeni, F. Pavanello, H. Gevorgyan, J. Notaros, L. Alloatti, M. T. Wade, C. Sun, S. A. Kruger, H. Meng, K. Al Qubaisi, I. Wang, B. Zhang, A. Khilo, C. V. Baiocco, M. A. Popović, V. M. Stojanović, and R. J. Ram, Integrating photonics with silicon nanoelectronics for the next generation of systems on a chip, Nature (London) **556**, 349 (2018).

[6] B. Shen, R. Polson, and R. Menon, Increasing the density of passive photonic-integrated circuits via nanophotonic cloaking, Nat. Commun. **7**, 13126 (2016).

[7] K. Okamoto, *Fundamentals of Optical Waveguides* (Elsevier Science & Technology, San Diego, CA, 2006).

[8] T. Ye, Y. Fu, L. Qiao, and T. Chu, Low-crosstalk Si arrayed waveguide grating with parabolic tapers, Opt. Express **22**, 31899 (2014).

[9] Y. Guo, Y. Guo, C. Li, H. Zhang, X. Zhou, and L. Zhang, Integrated optical phased arrays for beam forming and steering, Appl. Sci. **11**, 4017 (2021).

[10] A. Shafiee, S. Banerjee, K. Chakrabarty, S. Pasricha, and M. Nikdast, LoCI: An analysis of the impact of optical loss and crosstalk noise in integrated silicon-photonic neural networks, in *Proceedings of the Great Lakes Symposium on VLSI 2022* (Association for Computing Machinery, Irvine, CA, 2022), pp. 351–355.

[11] W. Song, R. Gatdula, S. Abbaslou, M. Lu, A. Stein, W.Y.-C. Lai, J. Provine, R.F.W. Pease, D. N. Christodoulides, and W. Jiang, High-density waveguide superlattices with low crosstalk, Nat. Commun. **6**, 7027 (2015).

[12] N. Yang, H. Yang, H. Hu, R. Zhu, S. Chen, H. Zhang, and W. Jiang, Theory of high-density low-cross-talk waveguide superlattices, Photon. Res. **4**, 233 (2016).

[13] R. Gatdula, S. Abbaslou, M. Lu, A. Stein, and W. Jiang, Guiding light in bent waveguide superlattices with low crosstalk, Optica **6**, 585 (2019).

[14] M. B. Mia, S. Z. Ahmed, I. Ahmed, Y. J. Lee, M. Qi, and S. Kim, Exceptional coupling in photonic anisotropic metamaterials for extremely low waveguide crosstalk, Optica **7**, 881 (2020).

[15] W. Ji, J. Luo, X. Zhou, H. Chu, H. Luo, W. Lu, and Y. Lai, Broadband low-crosstalk compact waveguides enabled by anisotropic metamaterial substrate, Opt. Express **33**, 28357 (2025).

[16] X. Yi, H. Zeng, S. Gao, and C. Qiu, Design of an ultra-compact low-crosstalk sinusoidal silicon waveguide array for optical phased array, Opt. Express **28**, 37505 (2020).

[17] H. Zafar, B. Paredes, J. Villegas, M. Rasras, and M. F. Pereira, O-band TE- and TM-mode densely packed adiabatically bent waveguide arrays on the silicon-on-insulator platform, Opt. Express **31**, 21389 (2023).

[18] P. Hildén and A. Shevchenko, Matrix analysis of high-density arrayed waveguides: Crosstalk suppression by bending, Phys. Rev. Appl. **22**, 024077 (2024).

[19] S. Maurya, R. Kolkowski, M. Kaivola, and A. Shevchenko, Crosstalk reduction between closely spaced optical waveguides by using higher-order modes, Phys. Rev. Appl. **18**, 044077 (2022).

[20] F. Yousry, P. Hildén, R. Kolkowski, and A. Shevchenko, Towards ultracompact photonic chips using higher-order modes in closely spaced waveguides, J. Phys. Photonics **7**, 045024 (2025).

[21] N. K. Efremidis and K. Hizanidis, Bandgap lattices: Low index solitons and linear properties, Opt. Express **13**, 10571 (2005).

[22] N. K. Efremidis, P. Zhang, Z. Chen, D. N. Christodoulides, C. E. Rüter, and D. Kip, Wave propagation in waveguide arrays with alternating positive and negative couplings, Phys. Rev. A **81**, 053817 (2010).

[23] J. M. Zeuner, M. C. Rechtsman, R. Keil, F. Dreisow, A. Tünnermann, S. Nolte, and A. Szameit, Negative coupling between defects in waveguide arrays, Opt. Lett. **37**, 533 (2012).

[24] N. K. Efremidis and D. N. Christodoulides, Discrete solitons in nonlinear zigzag optical waveguide arrays with tailored diffraction properties, Phys. Rev. E **65**, 056607 (2002).

[25] A. Szameit, T. Pertsch, S. Nolte, A. Tünnermann, and F. Lederer, Long-range interaction in waveguide lattices, Phys. Rev. A **77**, 043804 (2008).

[26] G. Wang, J. P. Huang, and K. W. Yu, Nontrivial Bloch oscillations in waveguide arrays with second-order coupling, Opt. Lett. **35**, 1908 (2010).

[27] M. A. Tapia-Valerdi, I. Ramos-Prieto, F. Soto-Eguibar, and H. M. Moya-Cessa, Waveguide arrays interaction to second neighbors: Semi-infinite case, Dynamics **5**, 51 (2025).

[28] M. A. Tapia-Valerdi, I. Ramos-Prieto, F. Soto-Eguibar, and H. M. Moya-Cessa, Waveguide arrays: Interaction to many neighbors, Dynamics **5**, 25 (2025).

[29] J. Schulz, C. Jörg, and G. Von Freymann, Geometric control of next-nearest-neighbor coupling in evanescently coupled dielectric waveguides, Opt. Express **30**, 9869 (2022).

[30] S. Longhi, Tunneling escape in optical waveguide arrays with a boundary defect, Phys. Rev. E **74**, 026602 (2006).

[31] T. Pertsch, T. Zentgraf, U. Peschel, A. Bräuer, and F. Lederer, Anomalous refraction and diffraction in discrete optical systems, Phys. Rev. Lett. **88**, 093901 (2002).

[32] S. Longhi, Discrete diffraction and shape-invariant beams in optical waveguide arrays, Phys. Rev. A **79**, 033847 (2009).

[33] Z. Mai, H. Xu, F. Lin, Y. Liu, S. Fu, and Y. Li, Dark solitons and grey solitons in waveguide arrays with long-range linear coupling effects, Appl. Sci. **7**, 311 (2017).

[34] M. Shams Solary, Toeplitz-plus-Hankel matrices with perturbed corners, Int. J. Nonlinear Anal. Appl. **13**, 3057 (2022).

[35] J. L. da Silva, Spectral properties for a type of heptadiagonal symmetric matrices, AIMS Math. **8**, 29995 (2023).

[36] M. J. Deen and P. Kumar Basu, *Silicon Photonics: Fundamentals and Devices* (John Wiley & Sons, Incorporated, Chichester, 2012).

[37] A. Hardy, W. Streifer, and M. Osiński, Coupled-mode equations for multimode waveguide systems in isotropic or anisotropic media, Opt. Lett. **11**, 742 (1986).

[38] W.-P. Huang, Coupled-mode theory for optical waveguides: An overview, J. Opt. Soc. Am. A **11**, 963 (1994).

[39] C. Xia, M. A. Eftekhar, R. A. Correa, J. E. Antonio-Lopez, A. Schülzgen, D. Christodoulides, and G. Li, Supermodes in coupled multi-core waveguide structures, IEEE J. Sel. Top. Quantum Electron. **22**, 196 (2016).

[40] Y. Yang, R. J. Chapman, B. Haylock, F. Lenzini, Y. N. Joglekar, M. Lobino, and A. Peruzzo, Programmable high-dimensional Hamiltonian in a photonic waveguide array, Nat. Commun. **15**, 50 (2024).

[41] Y. Shama, A. Hardy, and E. Marom, Multimode coupling of unidentical waveguides, J. Light. Technol. **7**, 420 (1989).

[42] M. D. Greenberg, *Ordinary Differential Equations* (John Wiley & Sons, Incorporated, Hoboken, NJ, 2012).

[43] M. L. Cooper and S. Mookherjea, Numerically-assisted coupled-mode theory for silicon waveguide couplers and arrayed waveguides, Opt. Express **17**, 1583 (2009).

[44] A. Sheveleva, M. Leonardo, C. Finot, and P. Colman, Local-field and effective-background effects in coupled integrated photonic waveguide systems, Phys. Rev. A **107**, 063502 (2023).

[45] T. Horikawa, D. Shimura, S.-H. Jeong, M. Tokushima, K. Kinoshita, and T. Mogami, The impacts of fabrication error in Si wire-waveguides on spectral variation of coupled resonator optical waveguides, Microelectron. Eng. **156**, 46 (2016).

[46] G. Bellanca, P. Orlandi, and P. Bassi, Assessment of the orthogonal and non-orthogonal coupled-mode theory for parallel optical waveguide couplers, J. Opt. Soc. Am. A **35**, 577 (2018).

[47] E. Kapon, J. Katz, and A. Yariv, Supermode analysis of phase-locked arrays of semiconductor lasers, Opt. Lett. **9**, 125 (1984).

[48] R. M. Gray, Toeplitz and circulant matrices: A review, Found. Trends Commun. Inf. Theory **2**, 155 (2005).

[49] S.-E. Ekström, C. Garoni, and S. Serra-Capizzano, Are the eigenvalues of banded symmetric Toeplitz matrices known in almost closed form? Exp. Math. **27**, 478 (2018).

[50] R. M. Beam and R. F. Warming, The asymptotic spectra of banded Toeplitz and quasi-Toeplitz matrices, SIAM J. Sci. Comput. **14**, 971 (1993).

[51] G. Dattoli, M. Migliorati, and H. M. Srivastava, Some families of generating functions for the Bessel and related functions, Georgian Math. J. **11**, 219 (2004).

[52] A. L. Jones, Coupling of optical fibers and scattering in fibers, J. Opt. Soc. Am. **55**, 261 (1965).

[53] K. G. Makris and D. N. Christodoulides, Method of images in optical discrete systems, Phys. Rev. E **73**, 036616 (2006).